Automatic techniques for evaluation of moiré deflectograms

J. A. Quiroga[a], J. Villa[a], D. Crespo[b].
[a] During the realisation of this work J. A. Quiroga was with
Centro de Investigaciones en Óptica, Loma del Pocito, s/n.
37150 León (Guanajuato, Mexico).
Telephone: 52 47 17 58 23. E-Mail: jvilla@andromeda.cio.mx, aq@fis.ucm.es
[b]Departamento de Óptica, Facultad de Ciencias Físicas, Universidad Complutense.
Ciudad Universitaria, s/n. 28040 Madrid (Spain).
Telephone: 34 91 394 4403. Fax: 34 91 394 4683.

ABSTRACT

In this work we present two methods for the analysis of moiré deflectograms. The first method is a Fourier-transform technique. The second method uses a regularization based method. Both methods are applied to realistic deflectograms and their performances are discussed.

Keywords: Moiré deflectometry, squared gratings, Fourier transform, regularization, phase-tracking

1. INTRODUCTION

Moiré deflectometry is a well-known technique for mapping ray deflections, based on Moiré and Talbot effects [1,2]. In the last years, several methods like phase-shifting algorithms and Fourier transform based techniques have been developed for the automatic extraction of information of moiré deflectograms [3,4]. The use of crossed gratings for the simultaneous acquisition of two independent information is a known procedure in shearing interferometry and experimental mechanics. In moiré deflectometry, the use of that kind of gratings allows the processing of two orthogonal ray deflections at the same time. In this work we present two different automatic methods for processing moiré deflectograms produced by that kind of crossed gratings and discuss their performances.

The first method is a Fourier transform technique [5] that allows the complete and automatic deflection characterization (in two orthogonal directions) of a phase object including automatic selection of the spatial carrier and the size of the filtering windows by using only two fringe patterns (a reference and a distorted pattern).

The second method uses the Regularized Phase-Tracking (RPT) technique [6]. A local regularization procedure based on the assumption that the fringe pattern is locally monochromatic, permits to obtain the phase already unwrapped and its gradients from a single fringe pattern.

In our particular case, the interest of the application is the determination of the power distribution in ophthalmic lenses. The basic set-up for moiré deflectometry is shown in figure 1. A collimated monochromatic coherent light beam illuminates the object to be tested, in our example a thin diverging lens L of focal length F. Behind it there are two squared Ronchi gratings G_1 and G_2. The observation plane P, is placed just behind the second grating. The separation between the gratings is denoted by Z. This work is organized as follows, in section 2 we discuss the basic equations appearing when squared gratings are used in moiré deflectometry. In section 3 the Fourier based method is presented. A short discussion about the regularized phase tracking as well as its application in the analysis of moiré deflectograms is depicted in section 4. In section 5 experimental results obtained by the two techniques are shown. Finally conclusions are given in section 6.

2. DEFLECTOMETRY WITH SQUARED GRATINGS

When squared gratings are used in a deflectometer as the one depicted in figure 1, a fringe pattern with two fringe systems containing the complete deflection information is obtained [5]. If we use Ronchi gratings, a model for this fringe pattern image may be expressed as

$$g(x,y) = \sum_{n=-\infty}^{\infty} a_n^{\,2} \cos[n\Phi_x(x,y)] \sum_{m=-\infty}^{\infty} b_m^{\,2} \cos[m\Phi_y(x,y)], \qquad (1)$$

SPIE Vol. 3744 • 0277-786X/99/$10.00

where

$$\Phi_x(x,y) = Zq\phi_x(x,y) + u_0 x + v_0 y\,, \tag{2}$$

and

$$\Phi_y(x,y) = Zq\phi_y(x,y) + v_0 x - u_0 y\,, \tag{3}$$

with $u_o=q(\cos\theta-1)$ and $v_o=q\sin\theta$, where Z is the distance between gratings, $q=2\pi/p$, p is the period of the grating, θ is the angle between the gratings and, ϕ_x and ϕ_y are the deflections we are looking for.

The selection of the component to be processed is by means of the carrier frequency which let us differentiate between ϕ_x and ϕ_y. For example if we chose as carrier $u_o x+v_o y$ we could obtain three fields corresponding to ϕ_x, $d\phi_x/dx$ and $d\phi_x/dy$

3. THE FOURIER TRANSFORM METHOD

As mentioned, the model for a squared grating deflectogram may be expressed as equation (1). From the frequency view point, this equation represents the information of the deflections centered at different points of the Fourier plane; that is, we can retrieve the two orthogonal deflections isolating its corresponding side lobe in the frequency plane by means of the carrier frequency and a suitable filter.

Following the analysis described by [5], we Fourier transform the distorted deflectogram and the reference (when no phase object is placed in the path of the collimated beam). To calculate ϕ_x we also calculate the inverse Fourier transform of the filtered distorted and reference to obtain

$$g_R(x,y) = b(x,y)\exp[i(u_0 x + v_0 y)], \tag{4}$$

and

$$g_I(x,y) = b(x,y)\exp[i(qZ\phi_x + u_0 x + v_0)]\,. \tag{5}$$

Dividing equation (5) by (4) we obtain the complex function,

$$g_x(x,y) = \exp[iqZ\phi_x(x,y)]\,. \tag{6}$$

And the phase map that corresponds to the deflection in the x direction is obtained by

$$\phi_x(x,y) = \frac{1}{qZ}\arctan\left(\frac{\mathrm{Im}[g_x(x,y)]}{\mathrm{Re}[g_x(x,y)]}\right), \tag{7}$$

In despite of its advantages, the Fourier transform method still have some problems. First, the boundaries of the area of interest are an important error source. This problem can be solved by using the Gerchberg extrapolation algorithm [7]. Second, the Fourier transform technique assumes the carrier to be constant. Iterative procedures can be used to minimize this problem [8]. Finally, the side lobes containing the deflection information must be isolated by a band-pass filter of given width. The size of the side lobe determines this width. If we want to recover the complete information contained in the side lobe, we cannot avoid that the noise present in this area is retrieved too. This problem may be solved if we use a narrow band -pass filter but this implies that the higher frequencies of the signal will be lost. The noise present in the recovered phase can be a drawback if gradient information must be computed, as is the case in the measurement of power distribution of ophthalmic lenses [9].

4. THE REGULARIZED PHASE TRACKING TECHNIQUE

In this section the application of the phase tracking technique [6] to retrieve the continuous deflection and its gradients from deflectograms obtained with squared gratings is presented. As we will show, this technique can solve the above-mentioned problems of the Fourier transform method while keeping its good properties.

The phase estimation of a fringe pattern may be formulated as an inverse problem that must be solved by an algorithm that incorporates a prior smoothness constraints about the phase being detected. To solve this problem we may regularize it by proposing a suitable cost function with two terms related to: first, the fidelity between the estimated function and the observations, and second, the smoothness of the phase being detected. It is assumed that the estimated phase function is the minimizer of the proposed cost function.

In the RPT technique developed by Servin et al. [6] the fringe pattern is considered as locally monochromatic, that is, the local irradiance is modeled as a cosinusoidal function phase modulated by a plane. The modeled cosinusoidal function must be close to the irradiance of the pattern which corresponds to the fidelity term. In this way, the phase must be adapted to every region in the pattern. Smoothness and continuity of the estimated phase are enforced by the regularization term. The cost functional proposed by Servin et al. is expressed as

$$U_T = \sum_{(x,y)\in L} U_{x,y}(\phi, \omega_x, \omega_y), \tag{8}$$

where

$$U_{x,y}(\phi, \omega_x, \omega_y) = \sum_{(\tilde{x},\tilde{y})\in(N_{x,y}\cap L)} [(g_h(x,y) - \cos[\phi_e(x,y,\tilde{x},\tilde{y}) + u_0 x + v_0 y])^2 + \ldots \\ \lambda[\phi(\tilde{x},\tilde{y}) - \phi_e(x,y,\tilde{x},\tilde{y})]^2 m(\tilde{x},\tilde{y})], \tag{9}$$

and

$$\phi_e(x,y,\tilde{x},\tilde{y}) = \phi(x,y) + \omega_x(x,y)(x-\tilde{x}) + \omega_y(x,y)(y-\tilde{y}). \tag{10}$$

Where $U_{x,y}$ is the energy of the system at a site (x,y) in the image. L is a two dimensional lattice that has valid data and $N_{x,y}$ is a neighborhood region around the coordinate (x,y) in the image where the phase is being detected. The field $m(x,y)$ is an indicator that equals 1 if the site has already been estimated and 0 otherwise. The fields ω_x and ω_y are the estimated local frequencies in the x and y directions that can be interpreted as the first derivatives of the phase; in this way, no differentiation over the estimated phase is required; and (u_o,v_o) stands for the components of the carrier frequency if present. The so called regularizing parameter λ controls the smoothness of the detected phase. $g_h(x,y)$ is a high-pass-filtered and normalized version of the fringe pattern. As Servin et al. mentioned, function (8) is multimodal, so it may have several minima, then the minimization of this function is a difficult task. Following Servin et al. we compute a first estimation of the phase by minimizing the local cost function (9) with the so called crystal-growing algorithm. Afterwards we improve the solution by applying the Iterated Conditional Mode (ICM) algorithm also described in [6].

The model used in the RPT (a single cosinusoidal function) differs from the model of the observed data (two crossed cosinusoidal functions). In this way when we select one of the fringe patterns by means of its carrier we are considering the other as noise which might introduce errors in the phase estimation. Servin et al. proposed the use of gradient descent method to minimize function (2). With squared gratings this simple algorithm is not robust enough even when the two deflections are clearly multiplexed in the frequency domain.

Taking into account the problem mentioned above, we decided to use a more efficient algorithm to minimize function (9). The selected minimizing algorithm was the Broyden-Fletcher-Goldfarb-Shanno. We have tested this algorithm with real images obtaining good results. The implementation of this algorithm is very easy as it is already included as a part of the optimization toolbox of the Matlab environment [10].

In the RPT technique the phase estimation is performed as a crystal growing process. This procedure is path dependent because the estimation depends on adjacent sites that have already been estimated; hence, the path selection for the crystal-growing process becomes important with noisy fringe patterns. The usual way to perform the crystal growing process is just scanning row by row. This procedure does not take into account the local quality of the fringe pattern. In the case of ophthalmic lenses the quality of the fringe pattern in the borders of the area of interest is very low. Also in the areas of high power there exists an increasing of the fringe density and therefore, a modulation decreasing due to the discrete sampling with finite size elements. For these reasons the crystal-growing algorithm must be able to select the path that process locally first the highest quality areas.

For this purpose, the quality-map-based algorithm of Ströbel [11] is applied for the crystal-growing process. The quality-map used by Ströbel is the amplitude modulation calculated by standard phase shifting. In our case we are analyzing single fringe patterns with a carrier; that is, there is no possibility to compute the amplitude map with phase shifting. However we can apply the Fourier transform technique and compute the amplitude map of the resulting complex signal. The best results were obtained by quantifying the quality map to a few values typically 4 or 5. As mentioned, one of the drawbacks of the Fourier transform method is the poor performance in the borders of the area of interest. That is, the computed quality map is not reliable in such borders. For this reason, additionally to the quantification, the zones adjacent to the borders are set to the lowest quality value. In this way, the borders are processed in last place.

5. EXPERIMENTAL RESULTS

In this section we show the results obtained with the two methods presented above. We have measured the spherical and cylindrical power of two progressive addition lenses.

In the particular case of ophthalmic lenses the most interesting parameters are the spherical and cylindrical power that can be computed from the partial derivatives of the deflection components [9]. If ϕ_x and ϕ_y are the deflection components, their partial derivatives are denoted by ϕ_{xx}, ϕ_{xy}, ϕ_{yy}, and ϕ_{yx}. From them the cylinder, C, and the sphere, S, are computed as

$$C = \sqrt{(\phi_{xx} + \phi_{yy})^2 - 4(\phi_{xx}\phi_{yy} - \phi_{xy}\phi_{yx})}, \tag{11}$$

and

$$S = \frac{1}{2}(\phi_{xx} + \phi_{yy} - C), \tag{12}$$

respectively.

The first sample is a Selective BBGR progressive addition lens. The image of the distorted deflectogram is shown in figure 2. Figures 3(a) and 3(b) show the contour maps obtained with the Fourier method of the cylindrical and spherical power (scaled in dioptries). We have compared the results of this method with the measurements made with a commercial focimeter. Figures 4(a) and 4(b) show the profile of the cylinder and the sphere along lines *AB* and *CD* of figures 3(a) and 3(b), together with the measurement made with a commercial focimeter along the same lines. The total processing time for image sizes of 512×512 is about one minute.

The second sample is a left eye Hoyalux progressive addition lens. The image of the distorted deflectogram is shown in figure 5. Figures 6(a) and 6(b) show the contour maps of the cylindrical and spherical power obtained with the RPT technique (scaled in dioptries). In the case of using the RPT no gradient calculation over the retrieved phase maps was necessary (i.e. it is implicit in the RPT algorithm). Figures 7(a) and 7(b) show the profile of the cylinder and the sphere along lines *AB* and *CD* of figures 6(a) and 6(b), together with the measurement made with a commercial focimeter along the same lines. The used value of λ in equation (9) was 5 in all the cases. The neighborhood size N_{xy} was 11×11 pixels in the first iteration and 13×13 pixels for the ICM iteration. The size of the images is 128×128. As mentioned, the use of a more sophisticated minimization algorithm implies a bigger processing time in our case the processing time was 20 minutes for each iteration, then to compute one deflection and two frequency fields we need about 40 minutes in a AMD K6-2 330 MHz computer equipped with 128 Mb of RAM.

6. CONCLUSIONS

We have presented two techniques for the automatic analysis of moiré deflectograms. The use of squared gratings allows the determination of two orthogonal deflection information within one image. The proposed Fourier method is well suited to process images with realistic sizes of about 512×512. The main problems of this technique are the poor performance in the borders of the area of interest, and the bad noise rejection due to the fixed bandwidth of the reconstruction filters, that makes very difficult the determination of the gradient fields from the recovered deflection phase. This is very important in applications as determination of power in ophthalmic lenses. As a solution to these problems we propose the use of a modified regularized phase tracking algorithm. The main drawback of this algorithm is the high processing time that due to the robust minimization algorithm needed for a good estimation of the gradient fields. The

reduction in the amount of processing time of the regularized phase tracking algorithm while keeping its good properties is a subject of our current research.

7. ACKNOWLEDGEMENTS

We want to thank the support of: a post-doctoral grant of the Universidad Complutense de Madrid, the "Becas Internacionales Flores-Valles" program, Spain; The Centro de Investigaciones en Optica (CIO), Mexico, the Consejo Nacional de Ciencia y Tecnologia (CONACyT), Mexico.

8. REFERENCES

1. A. W. Lohmann and D. E. Silva, "*An interferometer based on talbot effect*," Opt. Comm. 2, 413-415, (1971).
2. O. Kafri, and I. Glatt, *The Physics of Moiré Metrology* (Wiley, New York, 1989).
3. H. Canabal, J. A. Quiroga, and E. Bernabeu, *"Improved phase-shifting method for automatic processing of moire deflectograms,"* Appl. Opt. 37(26), 6227-6233, (1998).
4. M. Takeda and S. Kobayashi, *"Lateral aberration measurements with a digital Talbot interferometer,"* Appl. Opt. 23, 1760-1764 (1984).
5. J. A. Quiroga, D. Crespo and E. Bernabeu, "*Fourier transform method for automatic processing of moire deflectograms*,", Opt. Eng., in press.
6. M. Servin, J. L. Marroquin and F.J. Cuevas, "*Demodulation of a single interferogram by use of a two-dimensional regularized phase-tracking technique*," Appl. Opt. 36(19), 4540-4548 (1997).
7. C. Roddier, F. Roddier, *"Interferogram analysis using Fourier transform techniques,"* Appl. Opt. 26, 1668-1673 (1987).
8. J. Gu, F. Chen, *"Fast Fourier transform, iteration, and last-squares-fit demodulation image-processing of single-carrier fringe pattern,"* JOSA A, 10, 2159-2164 (1995).
9. J. Alonso, J. A. Gomez-Pedrero and E. Bernabeu, "*Local dioptric power matrix in a progressive addition lens*," Ophtal. Physiol. Opt. 17, 522-529 (1997).
10. *Matlab Optimization Toolbox*, user`s guide, version 5, The MathWorks Inc.
11. B. Ströbel, "*Processing of interferometric phase maps as complex-valued phasor images*," Appl. Opt. 35(13), 2192-2198 (1996).

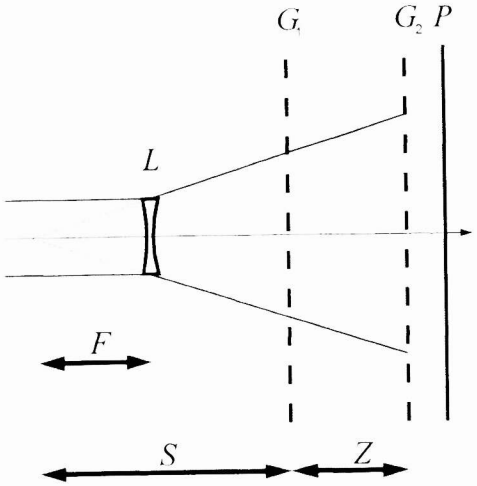

Figure 1. Experimental setup

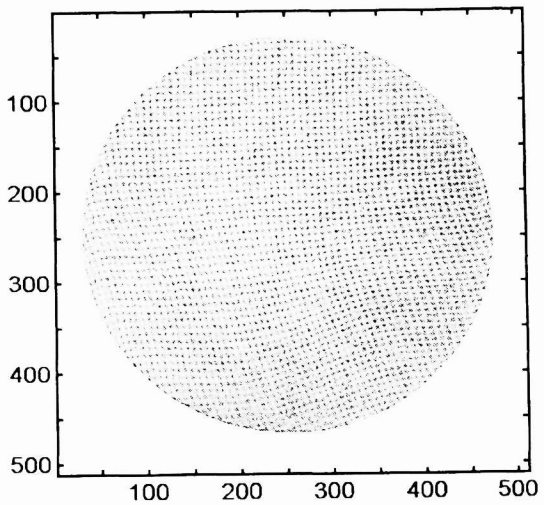

Figure 2. Deflectogram of the selective BBGR lens

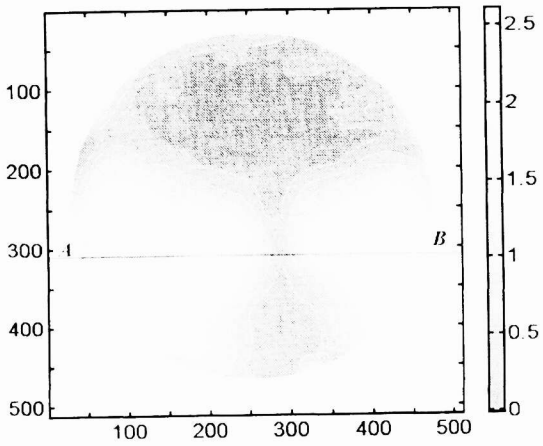

Figure 3a. Cilider (in D) of the selective BBGR

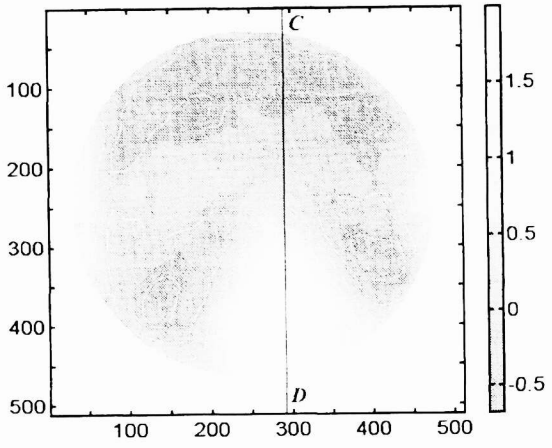

Figure 3b. Sphere (in D) of the selective BBGR

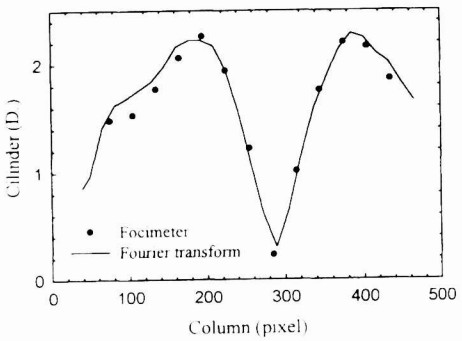

Figure 4a. Profile of the Cilinder along *AB*
Line in figure 3a

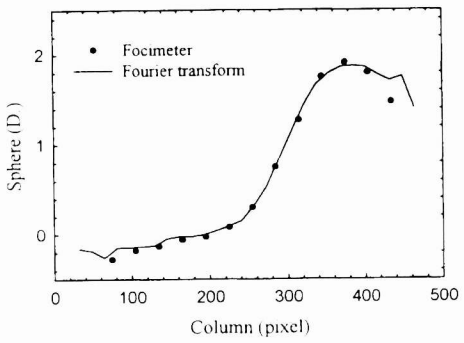

Figure 4b. Profile of the Sphere along *CD*
Line in figure 3b

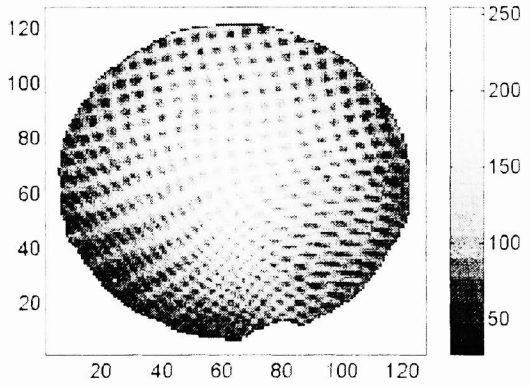

Figure 5. Deflectogram of the Hoyalux lens

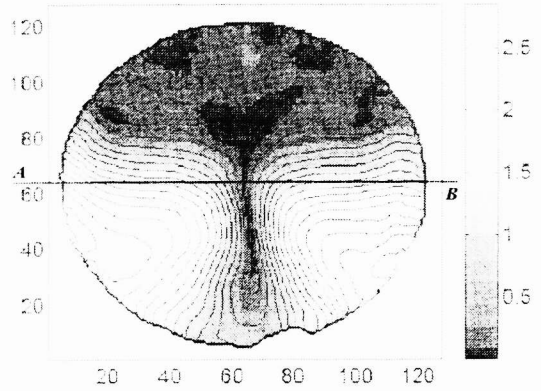

Figure 6a . Cilinder (in D) of the Hoyalux lens

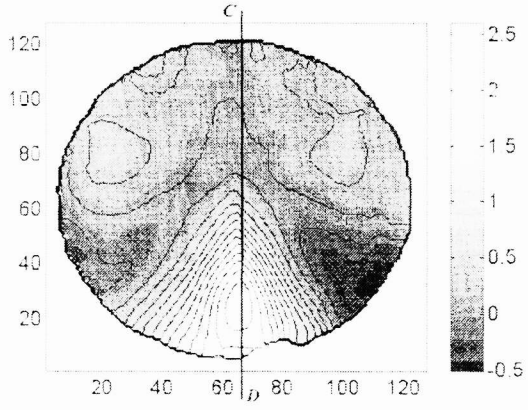

Figure 6b. Sphere (in D) of the Hoyalux lens

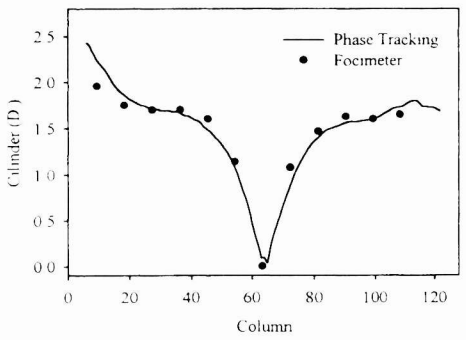

Figure 7a. Profile of the Cilinder along *AB* Line in figure 6a

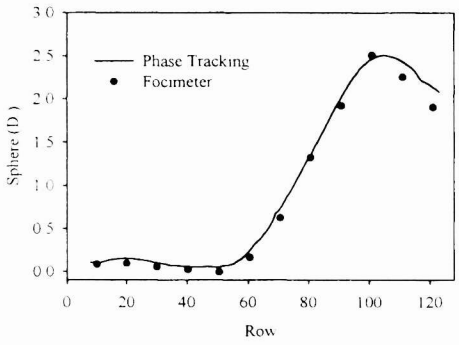

Figure 7b. Profile of the Sphere along *CD* Line in figure 6b